CHEMISTRY OF MATERIALS

pubs.acs.org/cm

Article

# Ultrathin One-Dimensional Molybdenum Telluride Quantum Wires Synthesized by Chemical Vapor Deposition

Youngdong Yoo,*[,⊥] Jong Seok Jeong,[⊥] Rui Ma, Steven J. Koester, and James E. Johns*

Cite This: *Chem. Mater.* 2020, 32, 9650−9655

Read Online

ACCESS | Metrics & More | Article Recommendations | Supporting Information

**ABSTRACT:** One-dimensional (1D) transition-metal chalcogenides (TMCs) are attracting increasing scientific and technological interest, especially for ultrasmall electronic interconnects and highly active catalysts. However, it is quite challenging to synthesize high-quality 1D TMCs over large areas on substrates. Here, we report on an atmospheric-pressure vapor-phase synthetic strategy for growing ultrathin 1D $Mo_6Te_6$ wires on various substrates such as $Si_3N_4$, $SiO_2$, and doped SiC, employing double $MoO_3$ sources. Scanning transmission electron microscopy confirms that the ultrathin 1D $Mo_6Te_6$ wires possessing thicknesses of 3−5 nm grow laterally to form wire networks. Lattice-resolution electron energy loss spectroscopy mapping clearly shows intensity variations of Mo-$M_{4,5}$ and Te-$M_{4,5}$ signals originating from Mo and Te atoms in the monoclinic $Mo_6Te_6$ structure. Furthermore, we investigate the vibrational modes of 1D $Mo_6Te_6$ wire networks, confirming that the two characteristic Raman peaks at 155 and 245 $cm^{-1}$ are associated with resonance Raman scattering. The 1D $Mo_6Te_6$ wire networks not only possess excellent transparency in the near-infrared range but also are electrically conductive. They also exhibit temperature-dependent Hall effects. We believe that these ultrathin 1D $Mo_6Te_6$ wires are auspicious materials for future electronics and catalysis.

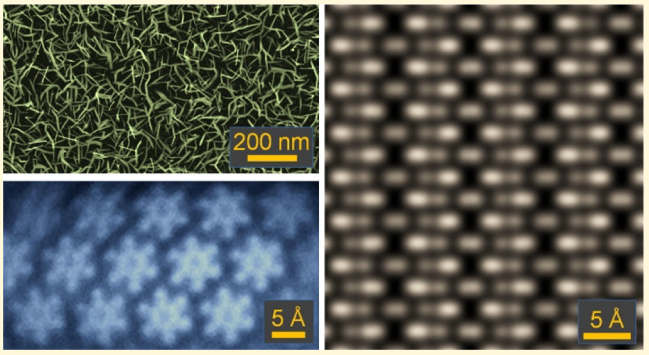




## INTRODUCTION

Atomically thin one-dimensional (1D) materials can possess unique physical and chemical properties originating from 1D quantum confinement of electrons and phonons.[1−5] These 1D properties can lead to various novel applications in electronics and catalysis and more scientifically interesting effects such as charge density waves and the potential for divergent thermal conductivity.[1,6−10] However, the synthesis of ultrathin 1D materials with diameters of a few nanometers is quite challenging due to their structural instability. Aside from carbon nanotubes with inherently stable 1D structures,[11] there have been only a few reports of stable ultrathin 1D materials possessing truly 1D geometry.[12−14] Recently, it has been reported that 1D transition-metal chalcogenide (TMC) wires with a formula of $M_6X_6$ (M: Mo or W and X: S, Se, or Te) can be stabilized in 1D geometry due to their inherent 1D crystal structure.[15−24] Irradiating a focused electron beam onto mechanically exfoliated 2D transition-metal dichalcogenides (TMDCs) or annealing exfoliated 2D TMDCs under ultrahigh vacuum has produced 1D TMC wires such as 1D $Mo_6S_6$, 1D $Mo_6Se_6$, and 1D $Mo_6Te_6$.[15−20] A few synthetic approaches including ultrahigh-vacuum molecular beam epitaxy also have created 1D TMC wires.[21−24] These 1D TMC wires with the backbone chain of transition-metal atoms covered by chalcogen atoms possess metallic characteristics due to the strong hybridization between transition-metal d and chalcogen p orbitals.[15,16]

Since the metallic 1D TMC wires can form ohmic contacts with semiconducting 2D TMDCs as well as have high mechanical stability,[25−29] they could be utilized as advanced ultrasmall electronic interconnects for high-performance 2D electronics by making edge contacts between 1D TMCs and 2D TMDCs.[15,30,31] In addition, the 1D TMC wires could also serve as highly active catalysts for various chemical reactions such as hydrogen evolution reactions because they have a very high surface-area-to-volume ratio due to their unique 1D geometry as well as possess a high density of surface transition-metal atoms which act as catalytic active sites.[32,33] To increase the potential uses of 1D TMC wires in these applications, it is highly desirable to develop a scalable simple synthetic strategy for producing high-quality 1D TMC wires chemically at atmospheric pressure.

Received: August 10, 2020
Revised: October 16, 2020
Published: October 30, 2020

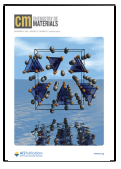

Here, we report on a scalable atmospheric-pressure chemical vapor deposition (APCVD) strategy for synthesizing 1D $Mo_6Te_6$ wires on a variety of substrates such as $Si_3N_4$, $SiO_2$, and doped SiC. It is clearly shown that 1D $Mo_6Te_6$ wires possess thicknesses of 3−5 nm and grow laterally to form wire networks on the substrates by scanning transmission electron microscopy (STEM). Power-dependent and wavelength-dependent Raman spectroscopy investigates two characteristic vibrational modes associated with resonance Raman scattering of 1D $Mo_6Te_6$ wire networks. Furthermore, the transmission and van der Pauw measurements confirm that the 1D $Mo_6Te_6$ wire networks with excellent transparency in the near-infrared range possess a sheet resistance of ∼4.94 kΩ/sq and exhibit temperature-dependent Hall effects.

## EXPERIMENTAL SECTION

**Synthesis.** 1D $Mo_6Te_6$ wire networks were synthesized using a horizontal tube furnace equipped with a vacuum pump and mass flow controllers. The detailed synthetic scheme is illustrated in Figure 1a.

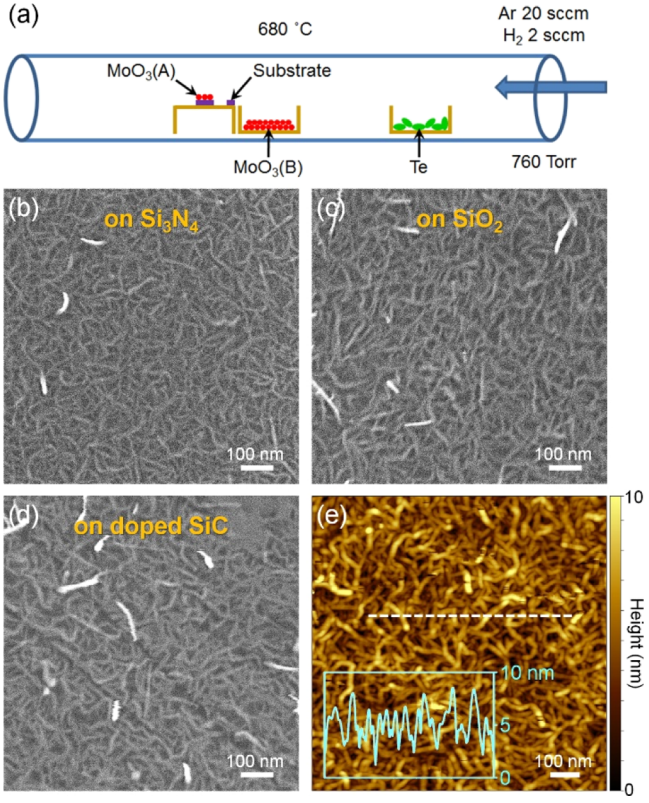


**Figure 1.** 1D $Mo_6Te_6$ wire networks grown on various substrates. (a) Schematic illustration of the experimental setup. (b−d) Scanning electron microscopy (SEM) images of 1D $Mo_6Te_6$ wire networks grown on $Si_3N_4$, fused silica ($SiO_2$), and doped SiC substrates, respectively. (e) Atomic force microscopy (AFM) height image and height line profiles of 1D $Mo_6Te_6$ wire networks grown on a $Si_3N_4$ substrate.

An alumina boat (50 × 20 × 20 mm, MTI Corporation) containing 400 mg of Te pieces (99.999%, Sigma-Aldrich) was placed upstream in a 3 in. diameter quartz tube. An alumina boat containing 400 mg of $MoO_3$ powder (≥99.5%, Sigma-Aldrich) was located at the center of the furnace. After a $MoO_3/SiO_2/Si$ substrate was prepared by drop-casting aqueous $MoO_3$ solution on a $SiO_2/Si$ substrate, both the substrate and the prepared $MoO_3/SiO_2/Si$ substrate were placed on an upside-down alumina boat, which was placed directly next to the boat containing the $MoO_3$ powder. After evacuating the tube to less than 100 mTorr, Ar and $H_2$ gases were supplied at rates of 20 and 2 sccm (standard cubic centimeters per minute), respectively. Under atmospheric pressure, the furnace was heated to 680 °C and was kept at 680 °C for 1 h. After the reaction, Ar gas was supplied at a rate of 500 sccm to purge any toxic gases, and the furnace was cooled down rapidly by opening the lid of the furnace.

**Characterization.** SEM images were taken using a JEOL JSM-6500F SEM operated at 5 kV. AFM measurements were performed in tapping mode on a Bruker NanoScope V MultiMode 8 SPM. X-ray photoelectron spectroscopy (XPS) spectra were taken using SSX-100 XPS with a monochromatic Al K$\alpha$ X-ray source operated at 200 W. Raman spectra were acquired using 532, 632, and 785 nm laser excitations focused through a 100× objective lens at room temperature. High-angle annular dark-field STEM (HAADF-STEM) data were taken using an aberration-corrected and monochromated FEI Titan G2 60-300 STEM operated at 200 keV. The convergence semi-angle of the incident probe was 23.5 mrad, and the inner angle of the HAADF detector was 57 mrad. Cross-sectional STEM specimens were fabricated using a FEI Helios NanoLab G4 dual-beam focused ion beam (FIB) operated at 30 kV. The specimens were thinned, and their damaged surfaces were removed by gallium ion milling operated at 1−5 kV. Electron energy loss spectroscopy (EELS) spectra were recorded using a Gatan Enfinium ER spectrometer, and energy-dispersive X-ray spectroscopy (EDS) spectra were taken using a Super-X system. Simulated HAADF-STEM images were obtained using the multislice method[34,35] with the parameters that were used in the experiments.

**Electrical Measurements.** Temperature-dependent electrical measurements were performed in a Janis cryostat using the van der Pauw geometry. Contacts were formed at the four corners of the square sample by sputtering 5 nm Al and 30 nm Au. The four-point resistance was measured in the temperature range from 80 to 300 K using a DC current excitation of 1 $\mu$A, and the sheet resistance was then calculated using the standard van der Pauw formula. The Hall resistance was measured at 100 and 300 K using an AC current excitation.

## RESULTS AND DISCUSSION

To synthesize 1D $Mo_6Te_6$ wire networks, we develop an APCVD method employing two sources of $MoO_3$ and a source of Te. A detailed synthetic scheme is illustrated in Figure 1a. The $MoO_3$(A) is a $MoO_3$ source located downstream next to a substrate on an upside-down alumina boat, which serves as a nucleation promoter. The second molybdenum source, $MoO_3$(B) is contained in an alumina boat located upstream adjacent to the upside-down alumina boat. $MoO_3$(B) is the main source of volatile $MoO_{3-x}$ vapor supplied to the substrate at the reaction temperature. The $MoO_{3-x}$ reacts with Te vapors to produce 1D $Mo_6Te_6$ wires on the substrate during the reaction. Control experiments confirm that both $MoO_3$(A) and $MoO_3$(B) are essential for the synthesis of 1D $Mo_6Te_6$ wires (Figure S1). We have synthesized 1D $Mo_6Te_6$ wires on various substrates using this method. SEM images show that dense 1D $Mo_6Te_6$ wires laterally grow on $Si_3N_4$, $SiO_2$, and doped SiC substrates to form 1D wire networks (Figure 1b−d). In addition to the laterally grown 1D $Mo_6Te_6$ wires, we also observe freestanding 1D $Mo_6Te_6$ wires which appear brighter in the SEM images. A tapping-mode AFM image and its height line profile show that 1D $Mo_6Te_6$ wires possess thicknesses of about 3−5 nm (Figure 1e).

In order to characterize the crystal structure and morphology of 1D $Mo_6Te_6$ wires, we perform HAADF-STEM on 1D $Mo_6Te_6$ wires that are directly synthesized on a 5 nm thick $Si_3N_4$ TEM grid (Figure S2). Low-magnification and high-magnification HAADF-STEM images show that dense 1D wires with thicknesses of about 3−5 nm constitute


https://dx.doi.org/10.1021/acs.chemmater.0c03264
Chem. Mater. 2020, 32, 9650−9655

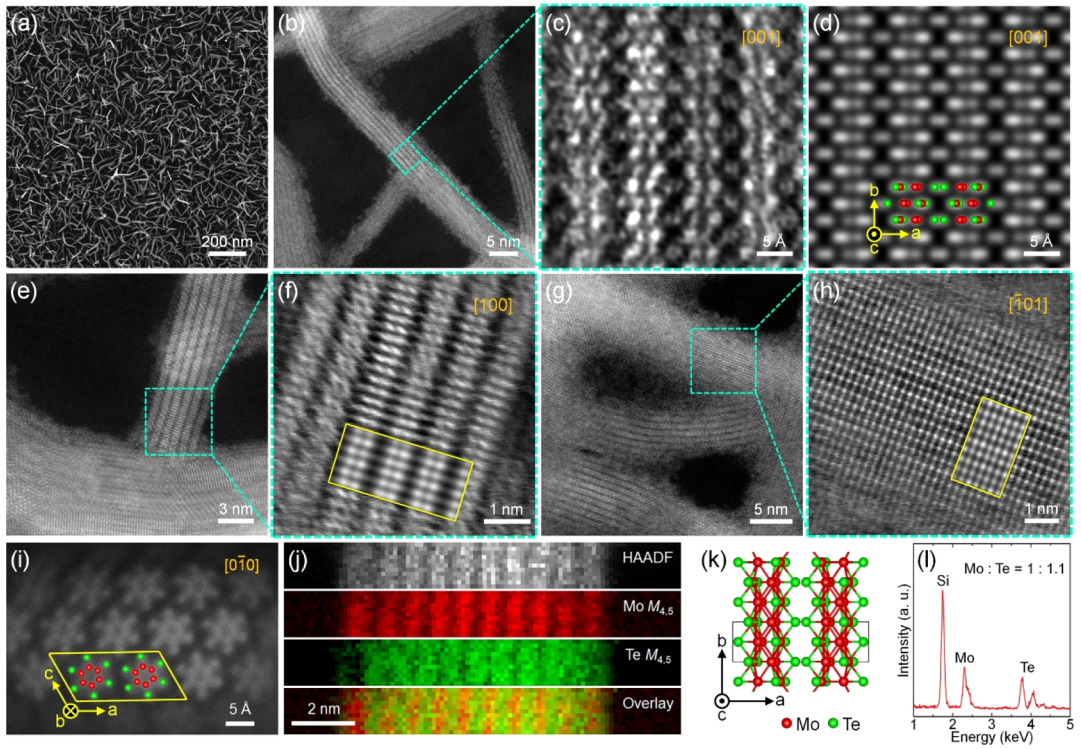


**Figure 2.** STEM analysis of 1D $Mo_6Te_6$ wire networks grown on a $Si_3N_4$ TEM grid. (a) Low-magnification HAADF-STEM image. (b) High-magnification HAADF-STEM image. (c) Zoom-in HAADF-STEM image of the dotted cyan square of (b). (d) Simulated HAADF-STEM image of monoclinic $Mo_6Te_6$ structure along the *c* axis with the superimposed unit-cell atomic model. (e–h) High-magnification and zoom-in HAADF-STEM images and superimposed simulated HAADF-STEM images (indicated by yellow squares) of 1D $Mo_6Te_6$ along the *a* axis and the [$\bar{1}$01] zone axis, respectively. (i) Cross-sectional HAADF-STEM image of a 1D $Mo_6Te_6$ wire along the *b* axis with the superimposed unit-cell atomic model. (j) EELS mapping of a 1D $Mo_6Te_6$ wire along the *c* axis. HAADF image, EELS maps of Mo-$M_{4,5}$ and Te-$M_{4,5}$ signals, and the overlay of the two EELS maps, respectively. (k) Atomic model of monoclinic $Mo_6Te_6$ structure along the *c* axis. The rectangle indicates the unit cell of the $Mo_6Te_6$ structure. (l) EDS spectrum showing that the Te/Mo atomic ratio is 1.1.

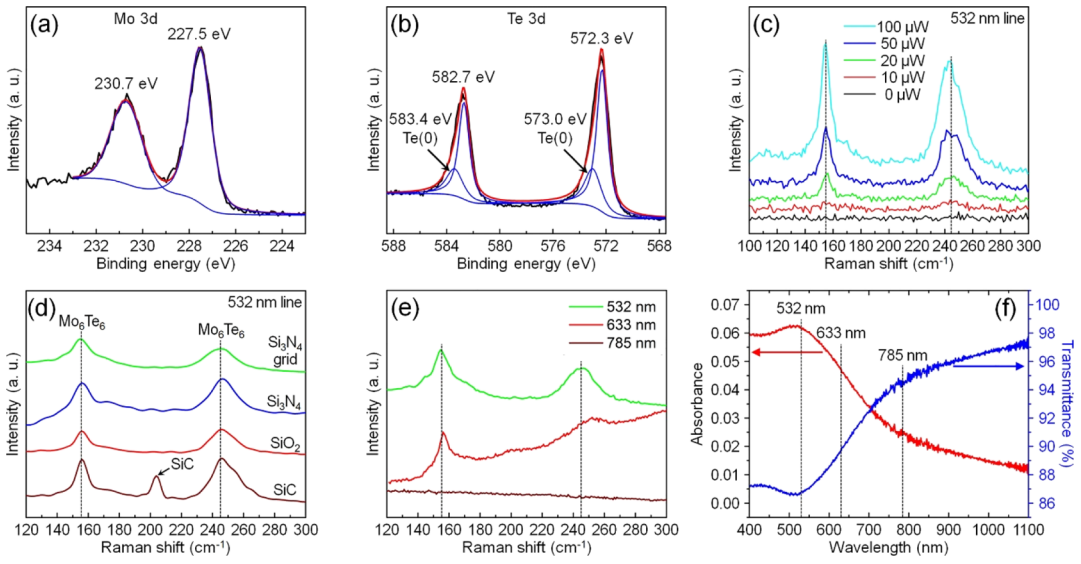


**Figure 3.** Chemical states and optical properties of 1D $Mo_6Te_6$ wire networks. (a,b) High-resolution XPS spectra showing Mo 3d and Te 3d peaks. (c) Raman spectra of 1D $Mo_6Te_6$ wire networks grown on a $Si_3N_4$ TEM grid, taken at 0, 10, 20, 50, and 100 $\mu$W with a 532 nm laser. (d) Raman spectra of the 1D $Mo_6Te_6$ wire networks grown on $Si_3N_4$ TEM grid, $Si_3N_4$, $SiO_2$, and SiC substrates taken at 100 $\mu$W. (e) Raman spectra of 1D $Mo_6Te_6$ wire networks grown on the $Si_3N_4$ TEM grid taken at 100 $\mu$W with 532, 633, and 785 nm lasers. (f) Absorbance and transmittance spectra of 1D $Mo_6Te_6$ wire networks grown on fused silica ($SiO_2$).

1D wire networks (Figure 2a,b). A zoomed-in HAADF-STEM image of the dotted cyan square of Figure 2b is in good agreement with the simulated HAADF-STEM image of monoclinic $Mo_6Te_6$ structure along the *c* axis (Figure 2c,d). Furthermore, HAADF-STEM images taken along the *a* axis and the [$\bar{1}$01] zone axis also correspond to the simulated


https://dx.doi.org/10.1021/acs.chemmater.0c03264
Chem. Mater. 2020, 32, 9650−9655

HAADF-STEM images (Figure 2e–h). Additional HAADF-STEM images and superimposed simulated HAADF-STEM images are provided in Figure S3. These HAADF-STEM images confirm the monoclinic $Mo_6Te_6$ structure with lattice parameters measured as follows: $a$ = 17.6 Å. $b$ = 4.5 Å, $c$ = 8.8 Å, and $\beta$ = 119°. To further confirm the crystal structure of the 1D $Mo_6Te_6$ wires, we have also carried out HAADF-STEM on the cross-sectional sample that was prepared by cutting the 1D $Mo_6Te_6$ wire along the plane perpendicular to the growth direction of the wire using a FIB technique. Cross-sectional HAADF-STEM imaging clearly shows that the wire composed of star-shaped $Mo_6Te_6$ unit clusters grows along the $b$ axis (Figure 2i).

We mapped the elemental composition using lattice-resolution EELS along the $c$ axis which shows a striped pattern constructed by intensity variations of Mo-$M_{4,5}$ and Te-$M_{4,5}$ signals (Figure 2j). Strong Te-$M_{4,5}$ signals are detected at the borders of star-shaped $Mo_6Te_6$ unit clusters, where only Te atoms are located without Mo atoms. Both Mo-$M_{4,5}$ and Te-$M_{4,5}$ signals are observed at the center of the star-shaped $Mo_6Te_6$ unit clusters, where both Mo and Te atoms exist. In order to show clearly where Mo and Te atoms are located in the 1D $Mo_6Te_6$ wire, the atomic model of monoclinic $Mo_6Te_6$ structure along the $c$ axis is illustrated in Figure 2k. The atomic model and its 3D perspective views along various crystallographic directions are shown in Figures S4 and S5. EELS spectra of Mo-$M_{4,5}$ and Te-$M_{4,5}$ signals that were used for the mapping are shown in Figure S6. An EDS spectrum and EDS mapping indicate that 1D $Mo_6Te_6$ wires have the Te/Mo atomic ratio of about 1.10 without any incorporation of unwanted atoms (Figures 2l and S7).

We perform XPS to analyze the elemental composition and the chemical states of 1D $Mo_6Te_6$ wires grown on a $Si_3N_4$ substrate (Figure 3a,b). In addition to Mo and Te signals, we detect C and O signals originating from contamination from air, which are used to calibrate the electron binding energies (Figure S8). High-resolution XPS spectra show that Mo 3d peaks are observed at 227.5 eV (Mo $3d_{5/2}$) and 230.7 eV (Mo $3d_{3/2}$) and Te 3d peaks are detected at 572.3 eV (Te $3d_{5/2}$) and 582.7 eV (Te $3d_{3/2}$), agreeing well with the previous report.[17] Interestingly, we also observe Te(0) peaks at 573.0 eV (Te $3d_{5/2}$) and 583.4 eV (Te $3d_{3/2}$), which could be attributed to elemental Te remaining on the substrate or on the surface of the 1D $Mo_6Te_6$ wires without reacting with Mo during the reaction. We assume that the elemental Te located on the surface of the 1D $Mo_6Te_6$ wires could play a role in stabilizing the 1D $Mo_6Te_6$ wires, but further studies are needed to confirm this. The Te/Mo atomic ratio of the 1D $Mo_6Te_6$ wires is calculated to be 1.09, indicating that the 1D $Mo_6Te_6$ wires are nearly stoichiometric.

We perform Raman spectroscopy to study the vibrational modes of 1D $Mo_6Te_6$ wires. We first carry out laser power-dependent Raman spectroscopy on the 1D $Mo_6Te_6$ wire networks grown on a $Si_3N_4$ TEM grid which have been thoroughly examined by HAADF-STEM. Raman spectra taken at 0, 10, 20, 50, and 100 $\mu$W with a 532 nm laser clearly show that the 1D $Mo_6Te_6$ wire networks exhibit two characteristic Raman peaks at 155 and 245 $cm^{-1}$ where their intensity increases linearly with increasing laser power (Figure 3c). The 1D $Mo_6Te_6$ wire networks grown on various substrates such as $Si_3N_4$, $SiO_2$, and doped SiC substrates also show the two characteristic Raman peaks under the 532 nm laser excitation (Figure 3d).

In addition to the 532 nm laser, 633 and 785 nm lasers are used to investigate laser-wavelength dependence of the two characteristic Raman peaks of the 1D $Mo_6Te_6$ wire networks grown on the $Si_3N_4$ TEM grid. The two characteristic Raman peaks appear at 157 and 249 $cm^{-1}$ under the 633 nm laser excitation, as they appear under the 532 nm laser excitation. However, no peak is observed under the 785 nm laser excitation (Figure 3e). These observations suggest that the two Raman characteristic peaks could be associated with resonance Raman scattering. The absorbance spectrum of the 1D $Mo_6Te_6$ wire networks grown on transparent fused silica ($SiO_2$) clearly shows that the 1D $Mo_6Te_6$ wire networks show an absorbance peak near 530 nm (Figure 3f, red curve), which could be due to electronic transitions of the 1D $Mo_6Te_6$ wire networks. Distinct from the 785 nm laser, the 532 and 633 nm lasers are close in energy to these electronic transitions, which could result in resonance Raman scattering to induce the two characteristic Raman peaks. A transmittance spectrum indicates that the 1D $Mo_6Te_6$ wire networks grown on fused silica ($SiO_2$) exhibit excellent transparency, especially in the near-infrared range from 800 to 1100 nm (Figure 3f, blue curve).

We propose the growth mechanism of 1D $Mo_6Te_6$ wires as follows. At the initial stage of the reaction, $MoO_{3-x}$ clusters arriving at the surface of the substrate from the vapor migrate and nucleate to form tiny $MoO_{3-x}$ crystals on the substrate. The nucleation process is facilitated by the $MoO_3$ nucleation promoters. At the same time, Te clusters reaching the surface of the substrate react with the tiny $MoO_{3-x}$ crystals to form tiny 1D $Mo_6Te_6$ wires. The $MoO_{3-x}$ and Te clusters continue to be supplied to the substrate surface, contributing to the axial growth of the 1D $Mo_6Te_6$ wires due to their inherent 1D crystal structure. We believe that very low Te flux is the key experimental condition for the synthesis of 1D $Mo_6Te_6$ wires because it leads to the exclusive formation of 1D $Mo_6Te_6$ wires by suppressing the formation of $MoTe_2$. We confirmed that 1D $Mo_6Te_6$ wires are exclusively synthesized without the formation of 2H and 1T′ $MoTe_2$ during the growth process (Figure S9). In addition, we confirmed that the 1D $Mo_6Te_6$ wires are uniformly synthesized over the whole substrate (Figure S10).

To investigate the electrical properties of 1D $Mo_6Te_6$ wire networks, we employ the van der Pauw method to perform temperature-dependent sheet and Hall resistance measurements. 1D $Mo_6Te_6$ wire networks grown uniformly on fused silica were used for the measurements. Cross-sectional HAADF-STEM images confirm that the 1D $Mo_6Te_6$ wire networks comprise 1D $Mo_6Te_6$ wires approximately 5 nm thick (Figure 4a,b). The coverage of the 1D $Mo_6Te_6$ wire networks is estimated to be about 20%. The 1D $Mo_6Te_6$ wire networks possess sheet resistances of 4.90–4.94 kΩ/sq in between 80 and 300 K (Figure 4c). Based on the estimated values of the thickness and coverage, the resistivity of the 1D $Mo_6Te_6$ wire networks is calculated to be $4.90 \times 10^{-4}$–$4.94 \times 10^{-4}$ Ω·cm. In addition, we measure the Hall resistance of the 1D $Mo_6Te_6$ wire networks as a function of magnetic field at 100 and 300 K. These results show that the 1D $Mo_6Te_6$ wire networks exhibit temperature-dependent Hall effects (Figure 4d,e). The carrier density of the 1D $Mo_6Te_6$ wire networks is calculated to be 2.75 ($\pm$0.1) $\times 10^{22}$ and 4.66 ($\pm$0.27) $\times 10^{22}$ $cm^{-3}$ at 100 and 300 K, respectively, confirming the metallic behavior of 1D $Mo_6Te_6$ wire networks.


https://dx.doi.org/10.1021/acs.chemmater.0c03264
Chem. Mater. 2020, 32, 9650–9655

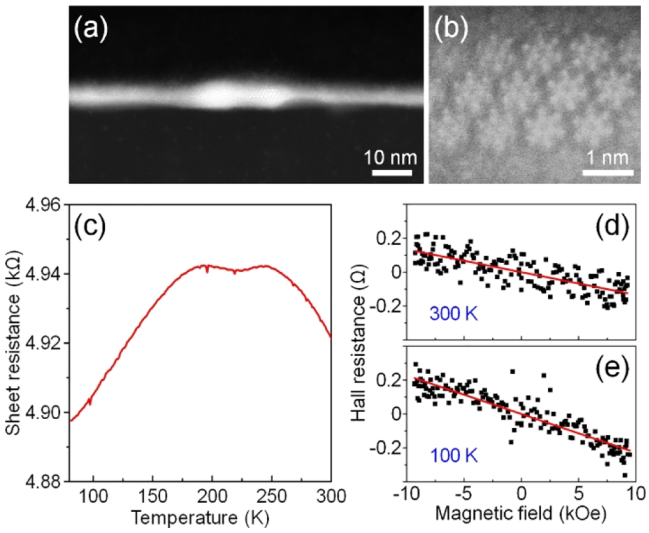


**Figure 4.** Electrical properties of 1D $Mo_6Te_6$ wire networks. (a,b) Low-magnification and high-magnification cross-sectional HAADF-STEM images of 1D $Mo_6Te_6$ wire networks grown on fused silica. (c) Temperature-dependent sheet resistance of the 1D $Mo_6Te_6$ wire networks. (d,e) Magnetic field-dependent Hall resistance of the 1D $Mo_6Te_6$ wire networks at 100 and 300 K, respectively.

## CONCLUSIONS

We have demonstrated that ultrathin 1D $Mo_6Te_6$ wires can be synthesized on a variety of substrates through chemical vapor deposition using two $MoO_3$ sources. The ultrathin 1D $Mo_6Te_6$ wires have thicknesses of 3−5 nm and grow laterally to form wire networks. Two characteristic Raman peaks are observed at 155 and 245 $cm^{-1}$ that are associated with resonance Raman scattering. The 1D $Mo_6Te_6$ wire networks are transparent in the near-infrared range as well as are electrically conductive. Furthermore, we have observed temperature-dependent Hall effects on the 1D $Mo_6Te_6$ wire networks. These ultrathin 1D $Mo_6Te_6$ wires are considered as advanced materials for flexible and transparent electronics and highly efficient catalysis.

## ASSOCIATED CONTENT

### Supporting Information

The Supporting Information is available free of charge at https://pubs.acs.org/doi/10.1021/acs.chemmater.0c03264.

Control experiments for synthesis of 1D $Mo_6Te_6$ wire networks; SEM images of 1D $Mo_6Te_6$ wire networks synthesized on a 5 nm thick $Si_3N_4$ TEM grid; HAADF-STEM images, fast Fourier transform patterns, and superimposed simulated HAADF-STEM images of 1D $Mo_6Te_6$ wire networks synthesized on a $Si_3N_4$ TEM grid; atomic model of monoclinic $Mo_6Te_6$ structure viewed along various crystallographic directions; 3D perspective views of $Mo_6Te_6$ atomic model viewed along various crystallographic directions; EELS spectra of 1D $Mo_6Te_6$ wire networks showing Mo-M and Te-M signals; EDS mapping of 1D $Mo_6Te_6$ wires grown on a $Si_3N_4$ TEM grid; XPS survey spectrum of 1D $Mo_6Te_6$ wire networks grown on a $Si_3N_4$ substrate; Raman spectra taken from the 1D $Mo_6Te_6$ wire networks grown on a $SiO_2$ substrate for 15, 30, 45, and 60 min, respectively; and Raman spectra taken at nine different positions on the same sample of 1D $Mo_6Te_6$ wire networks grown on a $SiO_2$ substrate (PDF)

## AUTHOR INFORMATION


### Corresponding Authors

**Youngdong Yoo** − *Department of Chemistry, Ajou University, Suwon 16499, Korea;* orcid.org/0000-0002-2916-2738; Email: yyoo@ajou.ac.kr

**James E. Johns** − *Department of Chemistry, University of Minnesota, Minneapolis, Minnesota 55455, United States;* orcid.org/0000-0001-6164-0384; Email: jjohns@umn.edu

### Authors

**Jong Seok Jeong** − *Department of Chemical Engineering and Materials Science, University of Minnesota, Minneapolis, Minnesota 55455, United States; Analytical Sciences Center, LG Chem Ltd., Daejeon 34122, Korea;* orcid.org/0000-0002-5570-748X

**Rui Ma** − *Department of Electrical and Computer Engineering, University of Minnesota, Minneapolis, Minnesota 55455, United States*

**Steven J. Koester** − *Department of Electrical and Computer Engineering, University of Minnesota, Minneapolis, Minnesota 55455, United States;* orcid.org/0000-0001-6104-1218

Complete contact information is available at: https://pubs.acs.org/10.1021/acs.chemmater.0c03264

### Author Contributions

⊥Y.Y. and J.S.J. contributed equally.


### Notes

The authors declare no competing financial interest.

## ACKNOWLEDGMENTS

We acknowledge the donors of the American Chemical Society Petroleum Research Fund (55709-DNI5) for funding and support of this research. This work was supported by the National Research Foundation of Korea (NRF) grant funded by the Korea government (MSIT) (nos. 2019R1C1C1008070 and 2018R1C1B5044670). S.J.K. and R.M. were supported by the Defense Threat Reduction Agency Basic Research through award no. HDTRA1-14-1-0042 and partially by the National Science Foundation (NSF) through the University of Minnesota MRSEC under award no. DMR-2011401. Portions of this work were conducted in the Minnesota Nano Center, which is supported by the NSF through the National Nanotechnology Coordinated Infrastructure, award no. ECCS-2025124.

## REFERENCES

(1) Sun, H.; Zhang, Y.; Zhang, J.; Sun, X.; Peng, H. Energy harvesting and storage in 1D devices. *Nat. Rev. Mater.* **2017**, *2*, 17023.
(2) Xia, Y.; Yang, P.; Sun, Y.; Wu, Y.; Mayers, B.; Gates, B.; Yin, Y.; Kim, F.; Yan, H. One-Dimensional Nanostructures: Synthesis, Characterization, and Applications. *Adv. Mater.* **2003**, *15*, 353−389.
(3) Cademartiri, L.; Ozin, G. A. Ultrathin Nanowires—A Materials Chemistry Perspective. *Adv. Mater.* **2009**, *21*, 1013−1020.
(4) Li, T.; Liu, Y.-H.; Porter, S.; Goldberger, J. E. Dimensionally Reduced One-Dimensional Chains of $TiSe_2$. *Chem. Mater.* **2013**, *25*, 1477−1479.
(5) Zhang, D.; Yu, Y.; Bekenstein, Y.; Wong, A. B.; Alivisatos, A. P.; Yang, P. Ultrathin Colloidal Cesium Lead Halide Perovskite Nanowires. *J. Am. Chem. Soc.* **2016**, *138*, 13155−13158.
(6) Wu, Z.; Chen, Z.; Du, X.; Logan, J. M.; Sippel, J.; Nikolou, M.; Kamaras, K.; Reynolds, J. R.; Tanner, D. B.; Hebard, A. F.; Rinzler, A. G. Transparent, Conductive Carbon Nanotube Films. *Science* **2004**, *305*, 1273−1276.

(7) Liu, G.; Rumyantsev, S.; Bloodgood, M. A.; Salguero, T. T.; Shur, M.; Balandin, A. A. Low-Frequency Electronic Noise in Quasi-1D $TaSe_3$ van der Waals Nanowires. *Nano Lett.* **2017**, *17*, 377−383.
(8) Vasylenko, A.; Marks, S.; Wynn, J. M.; Medeiros, P. V. C.; Ramasse, Q. M.; Morris, A. J.; Sloan, J.; Quigley, D. Electronic Structure Control of Sub-nanometer 1D SnTe via Nanostructuring within Single-Walled Carbon Nanotubes. *ACS Nano* **2018**, *12*, 6023−6031.
(9) Liu, X.; Liu, J.; Antipina, L. Y.; Hu, J.; Yue, C.; Sanchez, A. M.; Sorokin, P. B.; Mao, Z.; Wei, J. Direct Fabrication of Functional Ultrathin Single-Crystal Nanowires from Quasi-One-Dimensional van der Waals Crystals. *Nano Lett.* **2016**, *16*, 6188−6195.
(10) Zhang, Q.; Liu, C.; Liu, X.; Liu, J.; Cui, Z.; Zhang, Y.; Yang, L.; Zhao, Y.; Xu, T. T.; Chen, Y.; Wei, J.; Mao, Z.; Li, D. Thermal Transport in Quasi-1D van der Waals Crystal $Ta_2Pd_3Se_8$ Nanowires: Size and Length Dependence. *ACS Nano* **2018**, *12*, 2634−2642.
(11) Iijima, S. Helical microtubules of graphitic carbon. *Nature* **1991**, *354*, 56.
(12) Xu, H.; Liu, S.; Ding, Z.; Tan, S. J. R.; Yam, K. M.; Bao, Y.; Nai, C. T.; Ng, M.-F.; Lu, J.; Zhang, C.; Loh, K. P. Oscillating edge states in one-dimensional $MoS_2$ nanowires. *Nat. Commun.* **2016**, *7*, 12904.
(13) Cheng, F.; Xu, H.; Xu, W.; Zhou, P.; Martin, J.; Loh, K. P. Controlled Growth of 1D $MoSe_2$ Nanoribbons with Spatially Modulated Edge States. *Nano Lett.* **2017**, *17*, 1116−1120.
(14) Poh, S. M.; Tan, S. J. R.; Zhao, X.; Chen, Z.; Abdelwahab, I.; Fu, D.; Xu, H.; Bao, Y.; Zhou, W.; Loh, K. P. Large Area Synthesis of 1D-$MoSe_2$ Using Molecular Beam Epitaxy. *Adv. Mater.* **2017**, *29*, 1605641.
(15) Lin, J.; Cretu, O.; Zhou, W.; Suenaga, K.; Prasai, D.; Bolotin, K. I.; Cuong, N. T.; Otani, M.; Okada, S.; Lupini, A. R.; Idrobo, J.-C.; Caudel, D.; Burger, A.; Ghimire, N. J.; Yan, J.; Mandrus, D. G.; Pennycook, S. J.; Pantelides, S. T. Flexible metallic nanowires with self-adaptive contacts to semiconducting transition-metal dichalcogenide monolayers. *Nat. Nanotechnol.* **2014**, *9*, 436.
(16) Lin, J.; Zhang, Y.; Zhou, W.; Pantelides, S. T. Structural Flexibility and Alloying in Ultrathin Transition-Metal Chalcogenide Nanowires. *ACS Nano* **2016**, *10*, 2782−2790.
(17) Zhu, Z.; Wang, Q.; Zhang, C.; Addou, R.; Cho, K.; Wallace, R. M.; Kim, M. J. New $Mo_6Te_6$ Sub-Nanometer-Diameter Nanowire Phase from 2H-$MoTe_2$. *Adv. Mater.* **2017**, *29*, 1606264.
(18) Lehtinen, O.; Komsa, H.-P.; Pulkin, A.; Whitwick, M. B.; Chen, M.-W.; Lehnert, T.; Mohn, M. J.; Yazyev, O. V.; Kis, A.; Kaiser, U.; Krasheninnikov, A. V. Atomic Scale Microstructure and Properties of Se-Deficient Two-Dimensional $MoSe_2$. *ACS Nano* **2015**, *9*, 3274−3283.
(19) Zhu, H.; Wang, Q.; Cheng, L.; Addou, R.; Kim, J.; Kim, M. J.; Wallace, R. M. Defects and Surface Structural Stability of $MoTe_2$ Under Vacuum Annealing. *ACS Nano* **2017**, *11*, 11005−11014.
(20) Koh, A. L.; Wang, S.; Ataca, C.; Grossman, J. C.; Sinclair, R.; Warner, J. H. Torsional Deformations in Subnanometer MoS Interconnecting Wires. *Nano Lett.* **2016**, *16*, 1210−1217.
(21) Yu, Y.; Wang, G.; Tan, Y.; Wu, N.; Zhang, X.-A.; Qin, S. Phase-Controlled Growth of One-Dimensional $Mo_6Te_6$ Nanowires and Two-Dimensional $MoTe_2$ Ultrathin Films Heterostructures. *Nano Lett.* **2018**, *18*, 675−681.
(22) Nagata, M.; Shukla, S.; Nakanishi, Y.; Liu, Z.; Lin, Y.-C.; Shiga, T.; Nakamura, Y.; Koyama, T.; Kishida, H.; Inoue, T.; Kanda, N.; Ohno, S.; Sakagawa, Y.; Suenaga, K.; Shinohara, H. Isolation of Single-Wired Transition-Metal Monochalcogenides by Carbon Nanotubes. *Nano Lett.* **2019**, *19*, 4845−4851.
(23) Kanda, N.; Nakanishi, Y.; Liu, D.; Liu, Z.; Inoue, T.; Miyata, Y.; Tománek, D.; Shinohara, H. Efficient growth and characterization of one-dimensional transition metal tellurides inside carbon nanotubes. *Nanoscale* **2020**, *12*, 17185−17190.
(24) Kibsgaard, J.; Tuxen, A.; Levisen, M.; Lægsgaard, E.; Gemming, S.; Seifert, G.; Lauritsen, J. V.; Besenbacher, F. Atomic-Scale Structure of $Mo_6S_6$ Nanowires. *Nano Lett.* **2008**, *8*, 3928−3931.
(25) Venkataraman, L.; Lieber, C. M. Molybdenum Selenide Molecular Wires as One-Dimensional Conductors. *Phys. Rev. Lett.* **1999**, *83*, 5334−5337.
(26) Çakır, D.; Durgun, E.; Gülseren, O.; Ciraci, S. First principles study of electronic and mechanical properties of molybdenum selenide type nanowires. *Phys. Rev. B: Condens. Matter Mater. Phys.* **2006**, *74*, 235433.
(27) Popov, I.; Pecchia, A.; Okano, S.; Ranjan, N.; Di Carlo, A.; Seifert, G. Electronic and transport properties of contacts between molybdenum sulfide nanowires and gold electrodes. *Appl. Phys. Lett.* **2008**, *93*, 083115.
(28) Murugan, P.; Kumar, V.; Kawazoe, Y.; Ota, N. Assembling Nanowires from Mo−S Clusters and Effects of Iodine Doping on Electronic Structure. *Nano Lett.* **2007**, *7*, 2214−2219.
(29) Lee, R. S.; Kim, D.; Pawar, S. A.; Kim, T.; Shin, J. C.; Kang, S.-W. van der Waals Epitaxy of High-Mobility Polymorphic Structure of $Mo_6Te_6$ Nanoplates/$MoTe_2$ Atomic Layers with Low Schottky Barrier Height. *ACS Nano* **2019**, *13*, 642−648.
(30) Kappera, R.; Voiry, D.; Yalcin, S. E.; Branch, B.; Gupta, G.; Mohite, A. D.; Chhowalla, M. Phase-engineered low-resistance contacts for ultrathin $MoS_2$ transistors. *Nat. Mater.* **2014**, *13*, 1128−1134.
(31) Guimarães, M. H. D.; Gao, H.; Han, Y.; Kang, K.; Xie, S.; Kim, C.-J.; Muller, D. A.; Ralph, D. C.; Park, J. Atomically Thin Ohmic Edge Contacts Between Two-Dimensional Materials. *ACS Nano* **2016**, *10*, 6392−6399.
(32) Voiry, D.; Shin, H. S.; Loh, K. P.; Chhowalla, M. Low-dimensional catalysts for hydrogen evolution and $CO_2$ reduction. *Nat. Rev. Chem.* **2018**, *2*, 0105.
(33) Zhang, W.; Wang, J.; Zhao, L.; Wang, J.; Zhao, M. Transition-metal monochalcogenide nanowires: highly efficient bi-functional catalysts for the oxygen evolution/reduction reactions. *Nanoscale* **2020**, *12*, 12883−12890.
(34) Kirkland, E. J. *Advanced Computing in Electron Microscopy*, 2nd ed.; Springer: New York, 2010; p 289.
(35) Cowley, J. M.; Moodie, A. F. The scattering of electrons by atoms and crystals. I. A new theoretical approach. *Acta Crystallogr.* **1957**, *10*, 609−619.


https://dx.doi.org/10.1021/acs.chemmater.0c03264
*Chem. Mater.* 2020, 32, 9650−9655